Ideal Tensile Strength and Shear Strength of ZrO_2(111) / Ni(111) Ceramic-Metal Interface: A First Principles Study

Xingye Guo[a], Yi Zhang[a], Yeon-Gil Jung [b], Li Li[c], James Knapp [c], Jing Zhang [a,*]

a Department of Mechanical Engineering, Indiana University-Purdue University Indianapolis, Indianapolis, IN 46202, USA

b School of Materials Science and Engineering, Changwon National University, Changwon, Gyeongnam 641-773, Republic of Korea

c Praxair Surface Technologies Inc., Indianapolis, IN 46222, USA

*Corresponding author: jz29@iupui.edu

Abstract

The ideal mechanical strengths of ZrO_2(111)/Ni(111) ceramic-metal (C-M) interface are calculated through simulated tensile and shear deformations using the first principles calculations. The structures of ZrO_2(111)/Ni(111) interfaces with 1- and 3-layer Ni thicknesses are optimized and the mechanical properties are investigated. For tensile deformation in [111] direction, the Young's moduli of the 1-layer Ni and 3-layer Ni M-C models are 139.9 GPa and 60.2 GPa, respectively; and ultimate tensile strengths are 11.6 GPa and 7.9 GPa, respectively. For shear deformation in {111}<110> system, the shear moduli of the 1-layer Ni and 3-layer Ni M-C models are 43.9 GPa and 30.4 GPa, respectively; and ultimate shear strengths are 7.0 GPa and 3.0 GPa, respectively. For shear deformation in {111}<11$\bar{2}$> system, the shear moduli of the 1-layer Ni and 3-layer Ni M-C models are 30.9 GPa and 17.3 GPa, respectively; and ultimate shear strengths are 6.0 GPa and 1.8 GPa, respectively. Overall, 1-layer Ni C-M interface models have better mechanical properties than those of 3-layer models. The observed strengths are explained by using charge distribution, electron localization function, and Bader charge transfer analyses. The results are important for designing robust thermal barrier coating through optimizing bond coat thickness.

This is the author's manuscript of the article published in final edited form as:
Guo, X., Zhang, Y., Jung, Y.-G., Li, L., Knapp, J., & Zhang, J. (2016). Ideal tensile strength and shear strength of ZrO2(111)/Ni(111) ceramic-metal Interface: A first principle study. Materials & Design, 112, 254–262. https://doi.org/10.1016/j.matdes.2016.09.073

Keywords: Ceramic-metal (C-M) interfaces; first principles; mechanical property; deformation

1 Introduction

Ceramic-metal (C-M) interfaces have vast scientific and technological significance and are widely used in a variety of applications [1, 2]. An important example is thermal barrier coatings (TBCs) which are multi-layer ceramic-metallic coating systems to protect gas turbine components from heat at high temperatures. The multi-layer coating system typically consists of a ceramic top coat, an intermetallic bond coat (typically NiCrAlY), a thermally grown oxide (TGO) layer (in some cases, TGO does not exist in the as-sprayed coating), and a super nickel alloy substrate. Zirconia-based materials, e.g., 8% mol. yttria stabilized zirconia or 8YSZ, are the most widely used TBC top coats due to their low thermal conductivity, high melting point, similar coefficients of thermal expansion to that of super nickel alloy and bond coat, and good resistance to corrosion and thermal shock [3-5].

It is widely accepted that the mechanical properties at the C-M interface between the top and bond coats and/or between the top coat and the TGO layer have primary influence on the lifetime of the TBCs in the thermomechanical environments. It is still challenging to directly examine the interfacial mechanical properties from experiments. Modeling and simulation are powerful tools as an alternative way to investigate the interfacial properties and decipher failure mechanisms [6]. The failure and spallation mechanisms of the have been discussed by Evans in the context of continuum mechanics [7-9]. He suggested that the delamination, typically observed in TGO layer or near the interface, is related to a significant residual stress gradient which amplifies the imperfections in TBCs. Cracks propagate when the residual tensile and/or shear stresses exceed the delamination toughness of the top bond coat interface. At atomic level, the mechanical characteristics at the C-M interface are related to the intrinsic atomic properties. The idealized mechanical properties can be calculated which offers insights into the complex interface systems. Guo et al. investigated the mechanical properties of Ni (111) /α-Al2O3 (0001) interface, and calculated the theoretical shear strength and unstable stacking energy, using the first principles calculations [10]. Guo et al. found that the shear deformation of the Ni/ Al2O3 interfaces takes place by a successive breaking and rebonding process of the Al-O bond. Christensen et al. studied the adhesion energy of ZrO2 (111)/Ni (111) interface using the ultrasoft pseudopotential within the density functional theory [11]. The results showed that the monolayer ZrO2 (111) adheres relatively strong with the Ni substrate.

Although these previous effort, however, the exact mechanical properties of ZrO2/Ni interface are still not well examined. Specifically, the interfacial mechanical behaviors under tensile and shear stresses are not available. The difficulty of such studies primarily stems from the complexity of the interface structure, which requires minimizing the misfit between different crystal surfaces, and intensive calculations involved in the interfacial tensile and shear deformation simulations.

In this work, we conduct the first principles calculations of ZrO2 (111)/Ni (111) interface. An interface model in Ref. [11] is used to compare and/or partially validate the model through calculating the adiabatic work of adhesion. For mechanical property calculations, two Ni thickness of 1 and 3 atomic layers are modeled to investigate the effect of interface thickness on the mechanical properties. The crystallographic orientation (111) is considered since the primary slip system in face-centered cubic (fcc) metal crystals, such as Ni, is {111}<110>, with {111}<11$\bar{2}$> being the secondary slip system [12]. Although the actual slip systems of the ZrO2/Ni interface may be more complicated, both {111}<110> and {111}<11$\bar{2}$> should be the major slip systems. Therefore, the tensile stress-strain curve in <111> direction is calculated, and the shear stress-strain curves along {111}<110> and {111}<11$\bar{2}$> directions are computed. The toughness and elastic modulus, Young's modulus or shear modulus, are also calculated. Finally, the Bader charge analyses are conducted to explain the observed interfacial mechanical properties.

2 Computational methods

2.1 ZrO_2 (111)/Ni (111) interface model

The constructed ZrO_2 (111)/Ni (111) interface atomistic models are shown in Fig. 1. The cubic zirconia (*c*-ZrO_2) has the fluorite crystal structure (space group *Fm3m*) and Ni has a face-centered cubic (fcc) crystal structure (space group *Fm3m*). Both *c*-ZrO_2 and Ni small portions are cut from their bulk counterpart on (111) plane. To match the interface with minimal lattice misfit, the *c*-ZrO_2 and Ni small portions are rotated according to Ref. [11].

As shown in Fig. 1, the interface model contains two layers of ZrO_2 (111) atoms, and 1 or 3 layers of Ni (111) atoms. Because the O atoms and Zr atoms are not positioned in the same

horizontal plane, the termination of the ZrO_2 (111) surface may result in dipole moment perpendicular to the interface. Therefore, symmetric models are built to screen out the dipole interactions. Two ZrO_2 (111)/Ni (111) interfaces are in this interface model, corresponding to a sandwich structure. This model with the interface is extended periodically in three dimensions, due to the periodical boundary condition. To calculate adiabatic work of adhesion, ZrO_2 (111)/Ni (111) interface slabs are built with a vacuum layer thickness of 10 Å, which is large enough to eliminate the interaction between each interface film layer.

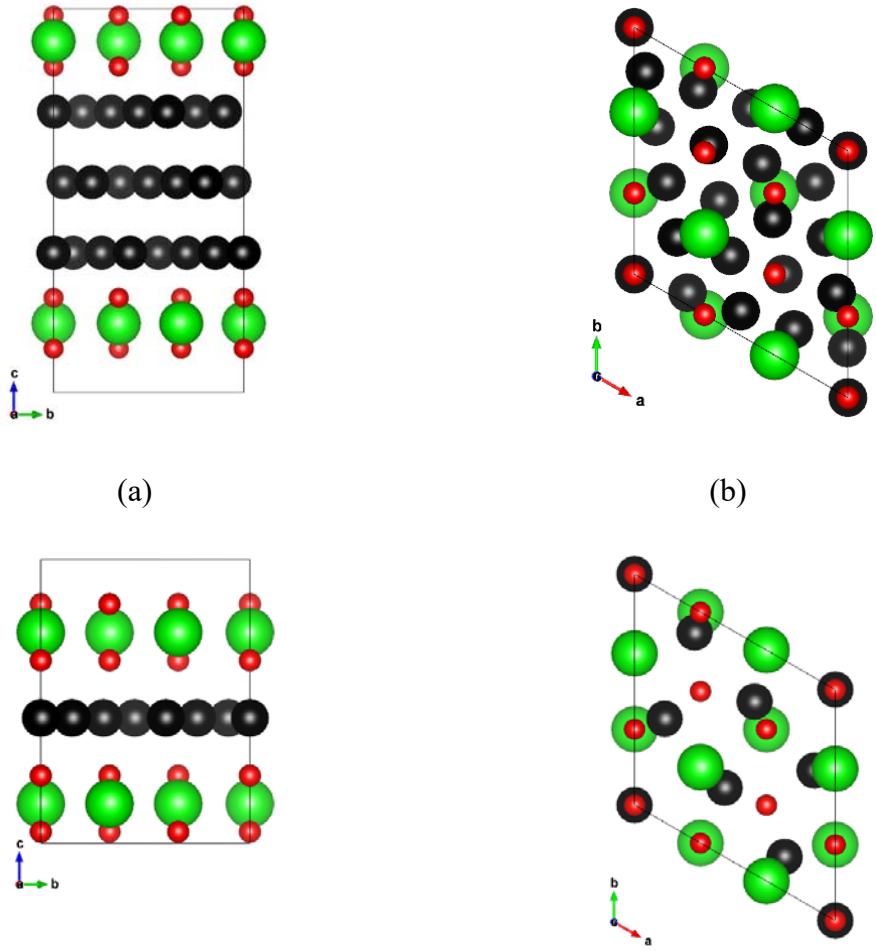

(a) (b)

(c) (d)

Fig. 1: ZrO_2 (111)/Ni (111) interface models with different Ni atomic layers: (a) side view and (b) top view with 3 layers of Ni, and (c) side view and (d) top view of 1 layer of Ni. Green, red, and black balls are Zr, O, and Ni atom, respectively (same coloring schemes are used in all figures afterwards).

The first principles calculations are carried out using the Vienna Ab initio Simulation Program (VASP) [13-15], based on the density functional theory (DFT) [16, 17].The projector augmented wave (PAW) method of generalized gradient approximation (GGA) functional is adopted to specify the exchange-correlation potential. A periodic supercell regime is used and *k*-point of the Brillouin zone is conducted using 3×3×1 Monkhost-Pack scheme. A conjugate-gradient algorithm is used to relax the ions into its instantaneous ground state. The plan-wave cutoff energy is 400 eV. The energy relaxation criterion for the electron is 10^{-5}eV for the self-consistency. The total forces are smaller than 0.01 eV/A in the ionic relaxation convergence criterion.

2.2 Adiabatic work of adhesion

In order to compare or partially validate the interface model, due to limited literature data, adiabatic work of adhesion (W_{adh}) is calculated using the atomistic model described in Ref. [11]. W_{adh} is the most commonly used property to describe the adhesion characteristics [11]:

$$W_{adh} = \frac{E_{0,Ni} + E^{N}_{0,Zro_2} - E^{N}_{Zro_2,Ni}}{A} \quad (1)$$

where $E_{0,Ni}$ and E_{0,ZrO_2} are the total energies of the relaxed Ni and ZrO_2 surfaces, respectively. $E_{ZrO_2,Ni}$ is the total energy of the relaxed ZrO_2/Ni interface structure. *A* is the area of the interface and *N* is the number of the ceramic layers [11].

2.3 Stress-strain behaviors in tensile and shear deformations

For tensile deformation, the calculations are conducted by extending the lattice parameters of the interface model in [111] direction, which is perpendicular to the interface. All ions in the interface model are relaxed, and the volume and the shape of the interface unit cell are also optimized during the stress tensor calculation process. Similarly, for shear deformations,

the shear stress is calculated by accumulating the shear strain in {111}<110> or {111}<112] direction [18].

2.4 Bader charge analysis

To explain the calculated stress-strain behaviors, the Bader method is used to calculate the charge transfer numbers and election density distributions [19-21]. The charge transfer results are processed by calculating the average charge difference between O and Ni ions. This is because the bonds formed in the ZrO_2/Ni interface models through the Zr and Ni atoms losing electrons, and the O atoms gaining electrons.

3 Results and discussion

3.1 Adiabatic work of adhesion

The relaxed ZrO_2 /Ni interface models for adiabatic work of adhesion calculations are shown in Fig. 2. In this work, all of the atoms except the two bottom Ni layers (which are away from the interface) are relaxed to allow to reach their equilibrium. Comparing with the structures in Ref. [11], the relaxed atomic structures in this study are slightly different. This is due to limited information regarding computation details in Ref. [11].

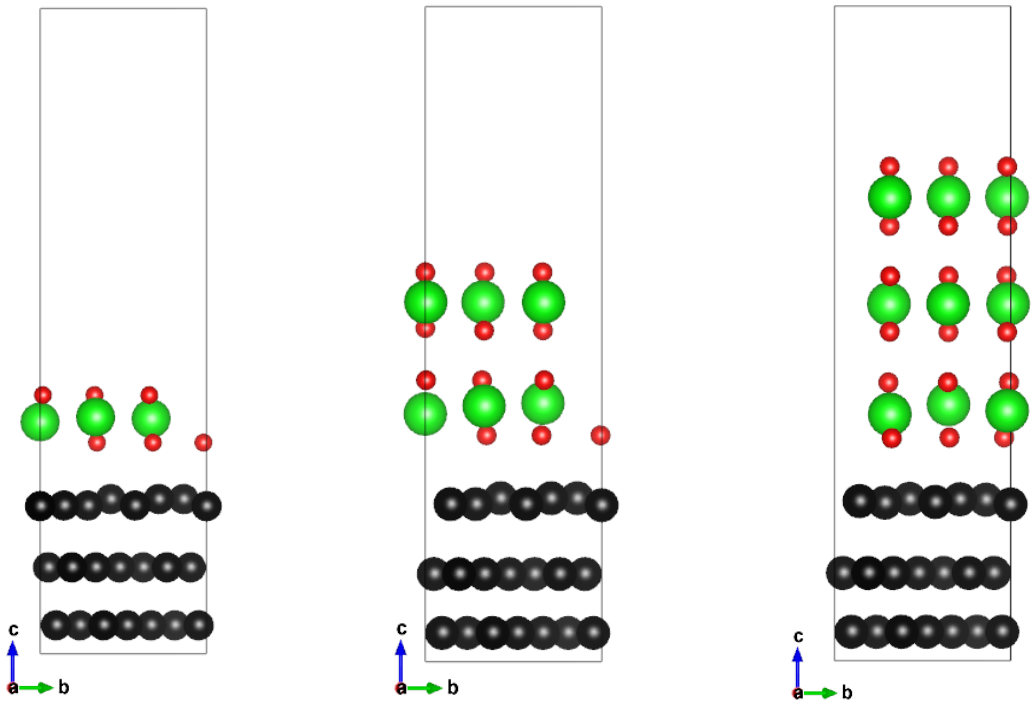

(a) (b) (c)

Fig. 2: Relaxed ZrO_2 (111)/Ni (111) interface models with a vacume layer above the slabs: (a) 1-layer ZrO_2, (b) 2-layer ZrO_2, and (c) 3-layer ZrO_2.

In this work, the calculated W_{adh} value of the interface with 1-layer ZrO_2 is 629 mJ/m2, which is greater than those of 2 and 3-layers ZrO_2 (554 mJ/m2 and 296 mJ/m2, respectively). In Ref. [11], the W_{adh} values are 2011, 1308, and 995 mJ/ m2 for 1, 2, and 3-layers ZrO2, respectively. Although our calculated values are lower than reported in Ref. [11] in ~ 60%, our calculated values follow the same trend as Ref. [11], i.e., a thicker ZrO2 layer corresponds to a lower adhesion energy.

3.2 Stress-strain behaviors in tensile and shear deformations

3.2.1 Tensile deformation along [111] direction

For mechanical property calculations, the atomic configurations of relaxed tensile models along [111] direction with Ni slabs of 1 and 3 layers are shown in Fig. 3 and Fig. 4, respectively.

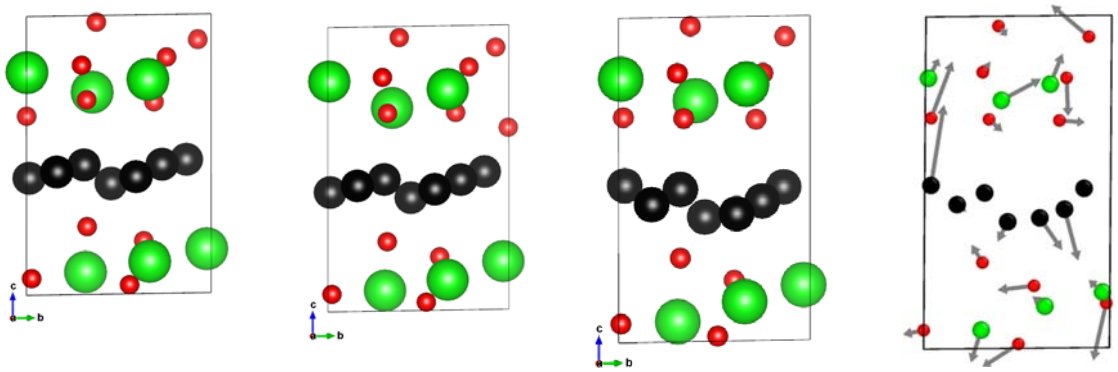

(a) (b) (c) (d)

Fig. 3: Tensile deformation models with 1 layer of Ni: (a) initial configuration, (b) strain of 0.051, (c) strain of 0.105, (d) atom displacement difference between configurations (c) and (a).

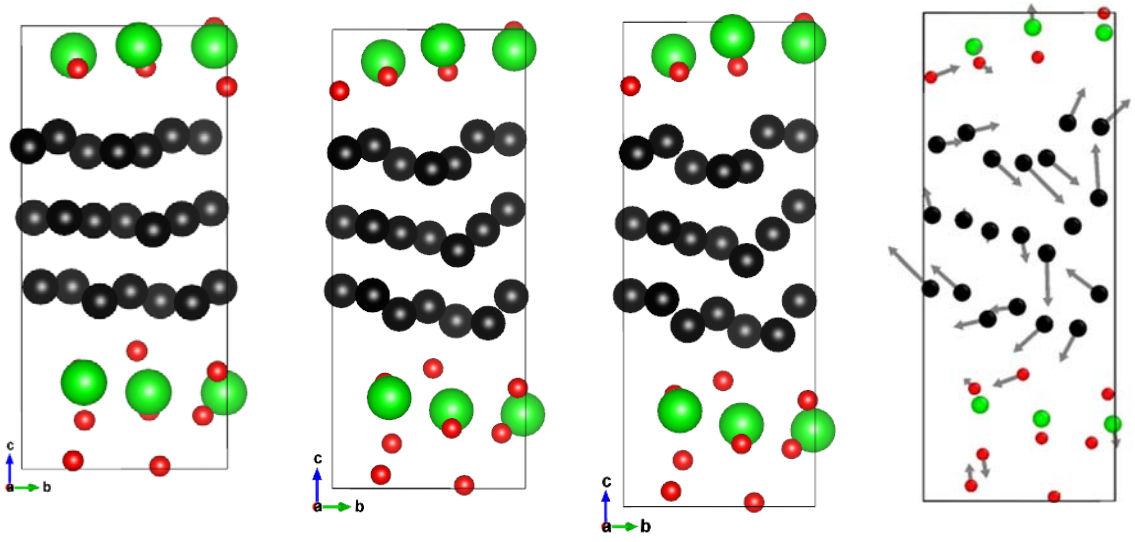

(a) (b) (c) (d)

Fig. 4: Tensile deformation models with 3 layers of Ni: (a) initial configuration, (b) strain of 0.072, (c) strain of 0.138, (d) atom displacement difference between configurations (c) and (a).

The tensile stress-strain curves of ZrO_2 (111)/Ni (111) interface with Ni slabs of 1 and 3 layers are shown in Fig. 5. As shown in Fig. 5, a thinner (1-layer) Ni layer has almost double Young's modulus (139.9 GPa) and higher ultimate tensile strength (11.6 GPa) than those of the 3-layer Ni case (60.3 GPa and 7.9 GPa, respectively) (see Table 1 for a complete summary of calculated mechanical properties, including elastic modulus, ultimate tensile/shear strength, and toughness). The layer-thickness dependence is consistent with work of adhesion values in Section 3.1, i.e., a thin Ni layer interface model has higher strength or work of adhesion.

In terms of deformation strain, the 3-layer Ni interface is more ductile as illustrated with larger tensile strain. This can be interpreted by the atom displacement vectors between the final and initial steps of the nanoscale tensile calculation, as shown in Fig. 3d and Fig. 4d for 1-layer and 3-layer Ni interface models, respectively. As shown in Fig. 4d, the atom displacements of Ni atoms at the interface are larger than that of Zr and O atoms in the 3-layer Ni interface model, suggesting most of the deformation occurs among the Ni layers in the 3-Ni-layers model. In the 1-layer Ni interface model, the atom displacements of Ni, Zr and O atoms are more randomly distributed than the 3-layer case, but the overall displacement is in the tensile direction. The 3-layer Ni interface has more plastic deformation than the 1-layer Ni interface, suggesting a thick Ni interface can provide extra deformation to accommodate tensile strain.

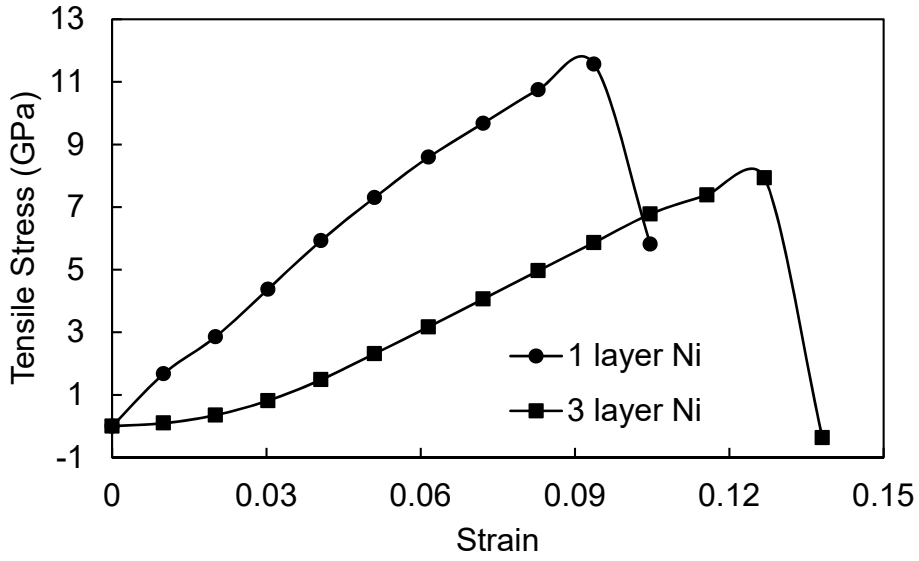

Fig. 5: Tensile stress-strain curves of ZrO_2(111)/Ni (111) interfaces with Ni slabs of 1 and 3 layers.

3.2.2 Shear deformations along {111}<110> and {111}<11$\bar{2}$> directions

The atomic configurations of 1-layer Ni slab model during shear deformations along {111}<110> and {111}<11$\bar{2}$> directions are shown in Fig. 6, and Fig. 7, respectively. The calculated shear stress-strain curves is given in Fig. 8. Both the shear modulus (43.9 GPa) and ultimate shear strength (7.9 GPa) along {111}<110> direction are greater than those along {111}<11$\bar{2}$> direction (30.9 GPa for shear modulus and 6.0 GPa for ultimate shear strength). Therefore, {111}<11$\bar{2}$> is a favorable shear slip system in this ZrO2 (111)/Ni (111) interface system, which is different from pure Ni. It is also noted that the ductility of {111}<110> measured by strain, 0.23, is lower than that of {111}<11$\bar{2}$>, 0.27.

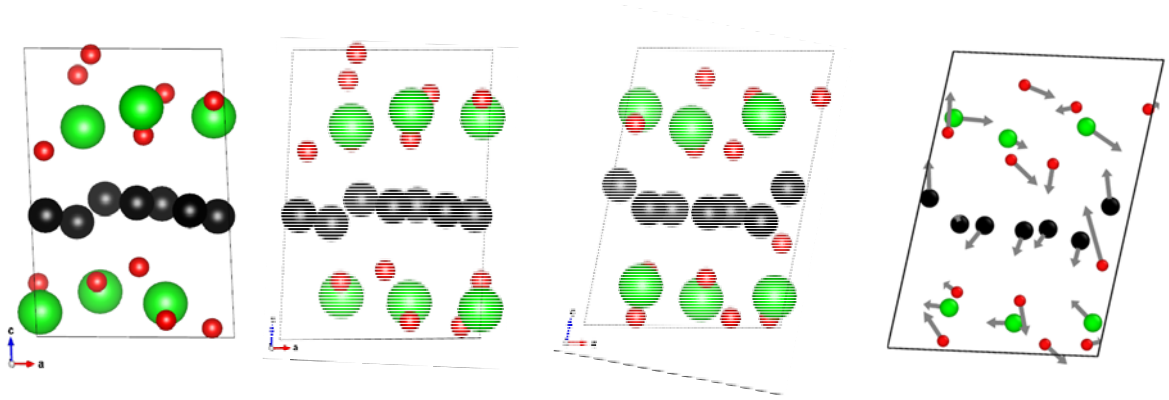

(a) (b) (c) (d)

Fig. 6: Shear deformation model with 1-layer Ni along {111}<110> direction after relaxation: (a) initial position, (b) strain 0.126, (c) strain 0.230, (d) atom displacement difference between configurations (c) and (a).

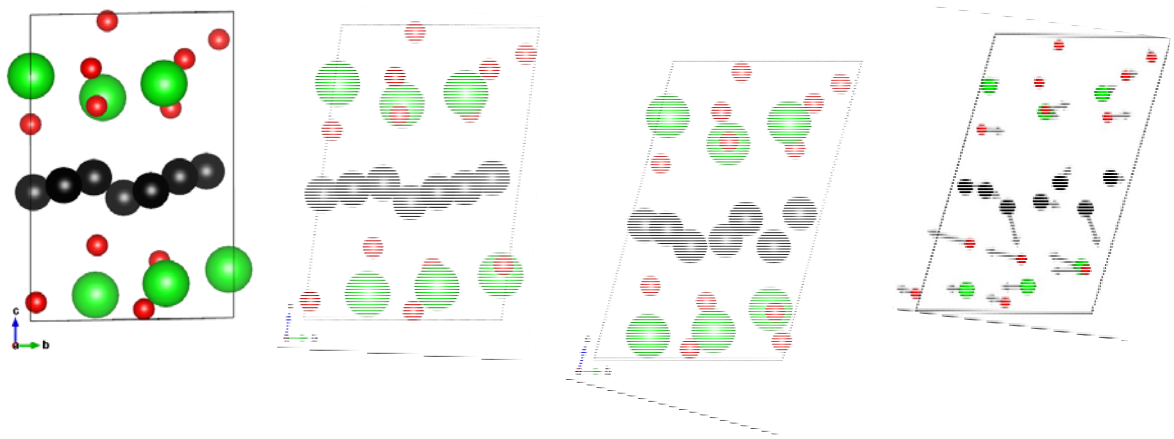

(a) (b) (c) (d)

Fig. 7: Shear deformation model with 1-layer Ni along {111}<11$\bar{2}$>direction after relaxation: (a) initial position, (b) strain 0.126, (c) strain 0.267, (d) atom displacement difference between configurations (c) and (a).

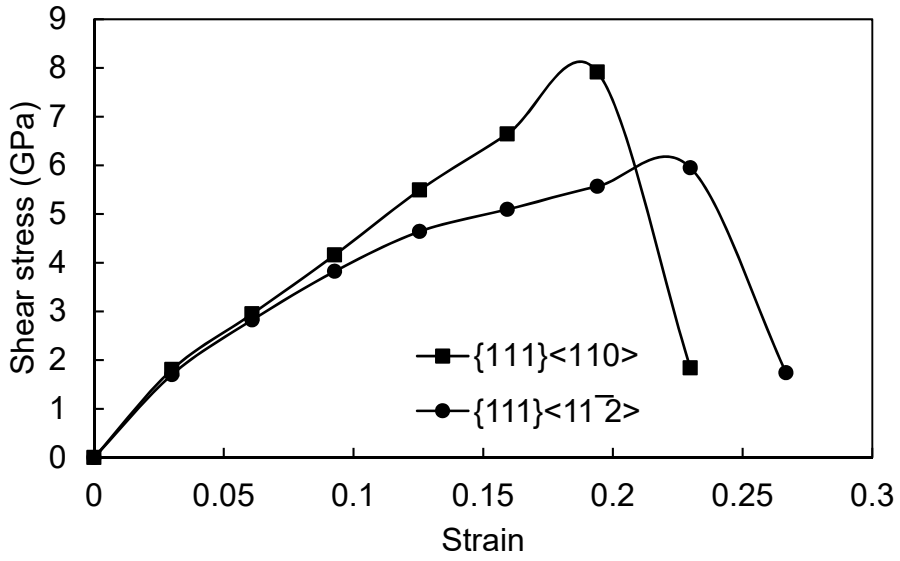

Fig. 8: Calculated shear stress-strain curves of 1-layer Ni shear deformation model.

The shear deformations along {111}<110> and {111}<11$\bar{2}$> directions of the 3-layer Ni model are shown in Fig. 9 and Fig. 10, respectively. The calculated shear stress-strain curves is given in Fig. 11. Similar to the 1-layer Ni model, for the 3-layer Ni, both the shear modulus (30.4 GPa) and ultimate shear strength (3.0 GPa) along {111}<110> direction are greater than those along {111}<11$\bar{2}$> direction (17.3 GPa for shear modulus and 1.8 GPa for ultimate shear strength). Therefore, {111}<11$\bar{2}$> is again a favorable shear slip system. Again, the ductility of {111}<110> measured by strain, ~0.10, is lower than that of {111}<11$\bar{2}$>, ~0.11.

Comparing with the 1-layer Ni shear deformation model, the shear moduli and strengths in the 3-layer model are much lower by 40%. This is because the shear deformation is primarily achieved by the deformation of Ni atoms. A thicker Ni layer allows to deformation at lower stress level.

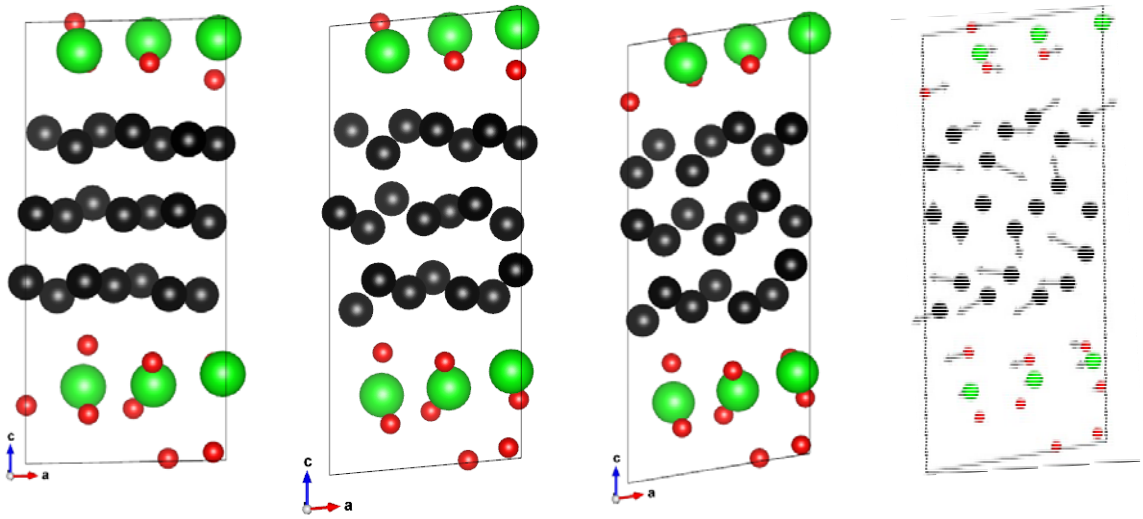

(a) (b) (c) (d)

Fig. 9: Shear deformation model with 3-layer Ni along {111}<110> direction after relaxation: (a) initial position, (b) strain 0.051, (c) strain 0.105, (d) atom displacement difference between configurations (c) and (a).

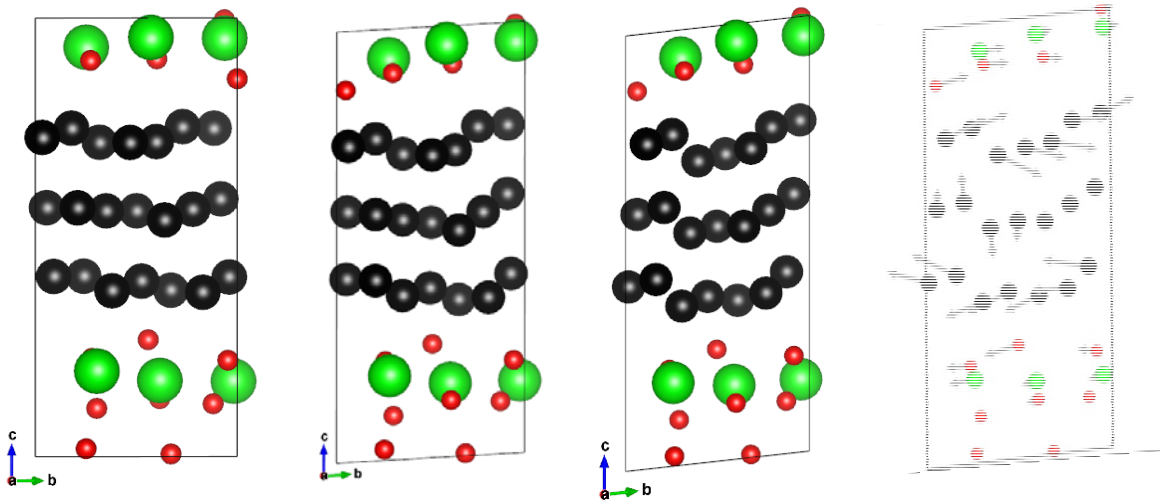

(a) (b) (c) (d)

Fig. 10: Shear deformation model with 3-layer Ni along {111}<11$\bar{2}$>direction after relaxation: (a) initial position, (b) strain 0.062, (c) strain 0.116, (d) atom displacement difference between configurations (c) and (a).

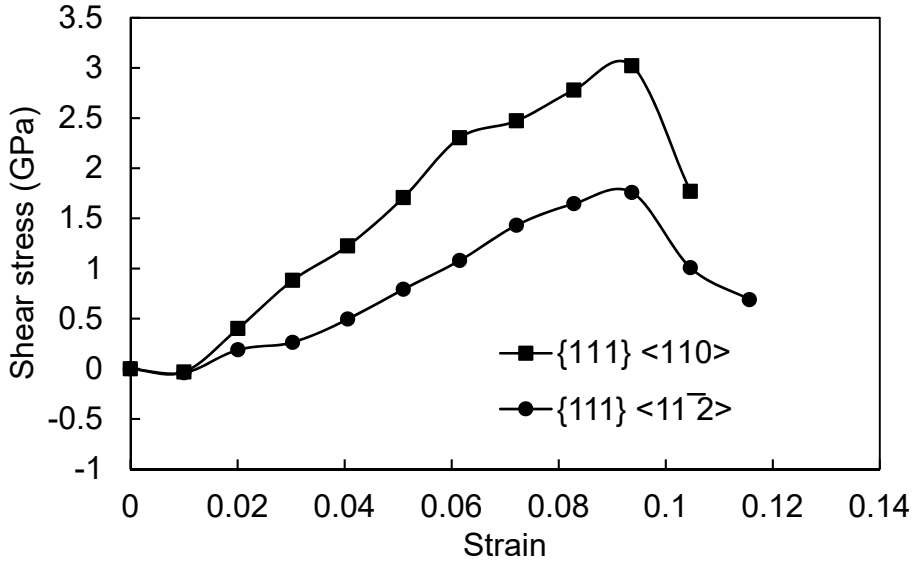

Fig. 11: Calculated shear stress-strain curves of 3-layer Ni shear deformation model.

The atom displacement vectors between final and initial step of the four shear deformation models are plotted in Fig. 6d, Fig. 7d, Fig. 9d and Fig. 10d. In the 1-layer Ni interface model, there are no obvious difference for the displacement vectors between Ni, Zr and O atoms, as shown in Fig. 6d and Fig. 7d. However, the displacement directions between the upper and lower ZrO_2/Ni interface are in the opposite directions, clearly demonstrating shear deformation mode. As shown in Fig. 9d and Fig. 10d, the 3-layer Ni interface models show a larger displacement in the Ni layers than that in the ZrO_2 layers, suggesting that the Ni layer provides the most deformation in these interface models.

In addition to stress, toughness can be used to measure the interfacial strength in large deformations. Toughness is calculated by integrating the are below the stress-strain curve. As shown in Table 1, the 1-layer Ni interface model has higher toughness than the 3-layer Ni model for both tensile and shear deformations. This is also consistent with the results from the adiabatic work of adhesion in section 3.1. In addition, the toughness in {111}<110> system is higher than that of {111}<11$\bar{2}$> direction for both 1-layer and 3-layer Ni models, primarily due to higher shear modulus and ultimate shear strength in the {111}<110> system.

It also suggests that the {111}<110> direction is stronger than that of {111}<11$\bar{2}$> direction during interface fracture.

Since most interfacial deformation is achieved by Ni atoms, it is worthy to compare the interfacial models with pure Ni. Ogata et al. calculated the shear stress-strain curves of pure Ni in {111}<11$\bar{2}$> direction using the DFT calculations [22]. The calculated ultimate strength is 5.1 GPa. It is similar to the 1-layer Ni interface model in this work, 6.0 GPa. However, the shear modulus in Ogata's work is ~ 60.3 GPa, which is larger than that in this work, 30.9 GPa. Comparing to experimental data, the Young's modulus of polycrystalline Ni (190 ~220 GPa) [23] is also much higher than that of ZrO2/Ni interface calculated in this work (139.9 GPa for 1-layer and 60.2 GPa for 3-layer Ni). Both elastic modulus and the ultimate strength values decrease as increase of the Ni layer thickness. These comparisons suggest that the strength of the ZrO2/Ni interface is substantially different from its pure component, and is determined by the Ni layer thickness.

Table 1: Calculated elastic modulus, ultimate strength, and toughness

Deformation mode, stress direction, and number of Ni layers	Elastic modulus (GPa)	Ultimate tensile/shear strength (GPa)	Toughness (MJ/m^3)
Tensile [111] 1-layer Ni	139.9	11.6	0.728
Tensile [111] 3-layer Ni	60.2	7.9	0.486
Shear {111}<110> 1-layer Ni	43.9	7.9	1.040
Shear {111}<110> 3-layer Ni	30.4	3.0	1.038
Shear {111}<11$\bar{2}$> 1-layer Ni	30.9	6.0	0.166
Shear {111}<11$\bar{2}$> 3-layer Ni	17.3	1.8	0.096

3.3 Charge density, electron localization function, and Bader charge analyses

The contours of charge density distribution are plotted in Fig. 12. As show in the figure, it is clear that the 1-layer Ni interface models (Fig. 12a, 12b, and 12c) have much strong O-Ni bonds than the 3-layer Ni cases (Fig. 12d, 12e, and 12f). This is the reason why the 1-layer Ni interface models have higher elastic modulus and strength.

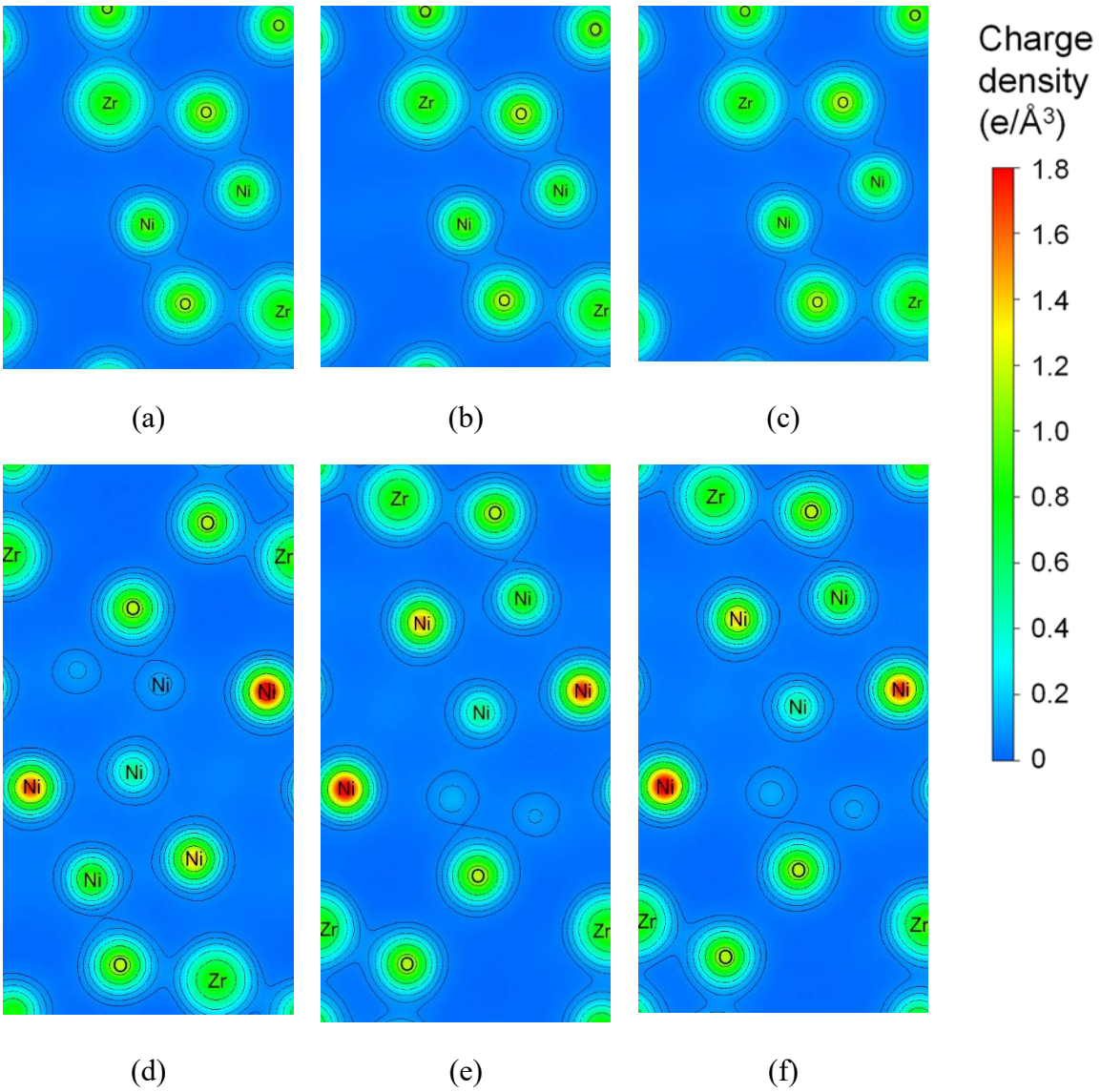

Fig. 12: Charge density distributions in logarithmic scale: (a) tensile <111> with 1-layer Ni, (b) shear {111}<110> with 1-layer Ni, (c) shear {111}<11$\bar{2}$> 1-layer Ni, (d) tensile <111> with 3-layer Ni, (e) shear {111}<110> 3-layer Ni, (f) shear {111}<11$\bar{2}$> 3-layer Ni.

The electron localization function (ELF) can be used to describe the electron localization status and bonding behaviors, which depend on the electron density, gradient, and the kinetic energy density [24, 25]. Typically the value of ELF ranges from 0 to 1, which specifies vaccum to perfect localization of the electrons. A higher ELF value in the ELF graph indicates the electrons are more localized. Metallic bonding in the ELF graph typically shows electron vacumm near the atom nucleus and a relative high electron localization value in areas far from the atom nucleus. Fig. 13 shows the ELF graph of the 1-layer and 3-layer Ni shear {111}<110> interface models. The ELF graphs in other tensile and shear cases have the similar patterns. The ELF of 3-layer Ni model shows electron vacum near the Ni atom, however it has a comparatively higher electron localizaiton value in space far from the Ni atoms. Additionally, the Ni layers in the interface model show a typical metalic bonding characteristcs, which can accomadate the deformation during the tensile and shear deformation process. This is consisitent with the charge density distribution analyses that a thicker Ni layer produces lower elastic modulus and lower untimate strength.

As shown in Fig. 13, the O and Zr atoms have higher ELF values than that of the Ni atoms in both 1-layer and 3-layer Ni interface models. The chemical bonding between the O and Ni atom at the interface shows an ionic bonding characteristics. In addition, both ELF graphs show a delocalized electron gap between the ZrO_2 and Ni layers, suggesting the ionic bonding might be weaker than the metallic bonding in Ni layer, which has higher ELF value than ionic bonding. During the tensile and shear processing, the ionic bonding becomes weaker, until it breaks. Because the 1-layer Ni models have stronger ionic bonding than that of the 3-layer Ni models, as shown in Fig. 12 of the charge density distribution contours, the 1-layer Ni interface models have higher ultimate strength that their 3-layer Ni counterparts.

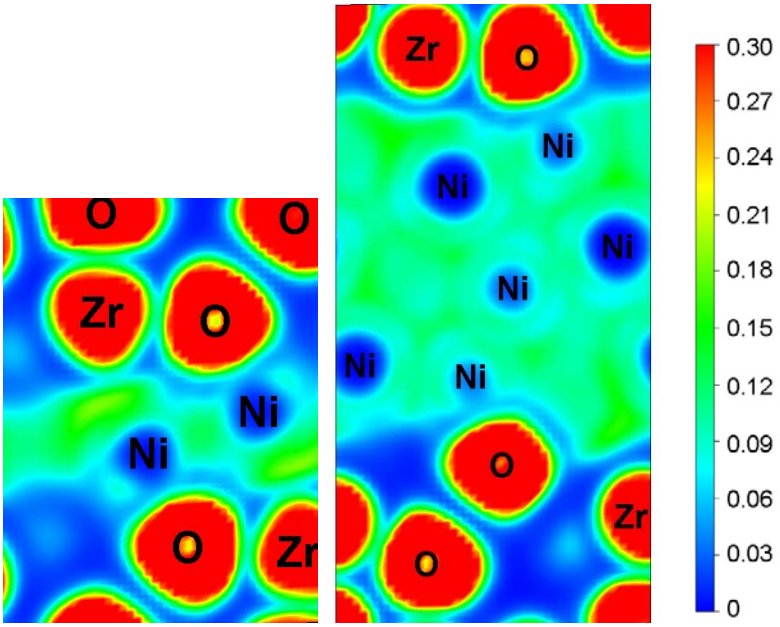

(a) (b)

Fig. 13: ELF graphs of (a) shear {111}<110> 1-layer Ni interface model, (b) shear {111}<110> 3-layer Ni interface model.

To get more quantitative measurements about bond characteristics, the average Bader charge numbers, including O, Zr, Ni ions, and the difference between O and Ni ions for both tensile and shear deformations, are summarized in Table 2. It is clear that the O and Ni differences, the average Bader charge difference between O and Ni ions of 1-layer Ni interface are consistently larger than those of 3-layer Ni interface in both tensile and shear cases. The Bader charge analysis results are also consistence with the charge density distributions in Fig. 12. A larger average Bader charge difference indicates stronger interaction between O and Ni, or more interaction between ZrO2 and Ni. This explains the higher ultimate strength and elastic modulus in the thin Ni layer interface than in the thick Ni layer interface, as shown in Table 1.

Table 2: Average Bader charge number (e)

Deformation mode, stress direction, and number of Ni layers	O	Zr	Ni	Difference between O and Ni
Tensile <111> 1-layer Ni	1.258	-2.457	-0.050	1.308
Tensile <111> 3-layer Ni	1.264	-2.459	-0.019	1.283
Shear {111}<110> 1-layer Ni	1.252	-2.451	-0.045	1.297
Shear {111}<110> 3-layer Ni	1.266	-2.462	-0.019	1.285
Shear {111}<11$\bar{2}$> 1-layer Ni	1.257	-2.460	-0.046	1.303
Shear {111}<11$\bar{2}$> 3-layer Ni	1.265	-2.460	-0.019	1.284

From the calculated mechanical properties of ZrO_2/Ni C-M interface, the layer thickness of bond coat film, NiCrAlY, at the interface makes a major impact on the coating's mechanical behavior. Typically, fracture or delamination in as-sprayed TBC system occurs near the interfaces between the top and bond coats [7, 26, 27]. Therefore, the mechanical properties near the interface are important to enhance the lifetime performance of TBC system. Higher toughness and elastic modulus at the interface enhance the ability of fracture resistance to impede crack propagations in the ceramic top coat near the interface. From the theoretical analyses of this work, the ultimate tensile and shear strength are decreased with increase of the bond coat film thickness at the interface, which means a thicker thickness of bond coat in TBC system corresponds to a weaker adhesion strength. On the other hand, a thin bond coat film will deteriorate the oxidation resistance of the TBC system. Therefore, the thickness of bond coat should be properly optimized to design and fabricate robust TBC systems.

4 Conclusion

The ideal tensile strength and shear strength of ZrO2(111)/Ni(111) C-M interface are calculated using the first principles calculations. The major conclusions are summarized below:

For tensile deformation in [111] direction, the Young's moduli of the 1-layer Ni and 3-layer Ni M-C models are 139.9 GPa and 60.2 GPa, respectively; the ultimate tensile strengths are 11.6 GPa and 7.9 GPa, respectively; the toughnesses are 0.728 MJ/m^3 and 0.486 MJ/m^3, respectively. The 1-layer Ni model shows higher mechanical strength than the 3-layer Ni model in tensile deformation.

For shear deformation in {111}<110> system, the shear moduli of the 1-layer Ni and 3-layer Ni M-C models are 43.9 GPa and 30.4 GPa, respectively; the ultimate shear strengths are 7.0 GPa and 3.0 GPa, respectively; the toughnesses are 1.040 MJ/m^3 and 1.038 MJ/m^3, respectively. The 1-layer Ni model shows higher mechanical strength than the 3-layer Ni model in shear deformation.

For shear deformation in $\{111\}\langle 11\bar{2}\rangle$ system, the shear moduli of the 1-layer Ni and 3-layer Ni M-C models are 30.9 GPa and 17.3 GPa, respectively; the ultimate shear strengths are 6.0 GPa and 1.8 GPa, respectively; the toughnesses are 0.166 MJ/m^3 and 0.096 MJ/m^3, respectively.

Both charge distribution and Bader charge analyses show that the 1-layer Ni C-M model has stronger interaction between Ni and O ions than that of the 3-layer Ni model, which explains the higher mechanical properties in 1-layer Ni model from the calculated tensile and shear stress-strain results.

From the theoretical analyses of this work, the ultimate tensile and shear strength are decreased with increase of the bond coat film thickness at the interface, which means a thicker thickness of bond coat in TBC system corresponds to a weaker adhesion strength. On the other hand, a thin bond coat film will deteriorate the oxidation resistance of the TBC system. Therefore, the thickness of bond coat should be properly optimized to design and fabricate robust TBC systems.

Acknowledgment

J.Z. acknowledges the financial support provided by the United States Department of Energy (Grant No. DE-FE0008868, program manager: Richard Dunst) and IUPUI RSFG and IDRF grants. Y.J. acknowledges the financial support provided by the National Research Foundation of Korea (NRF) Grant funded by the Korean Government (MEST) (2011–0030058), by the Power Generation & Electricity Delivery of the Korea Institute of Energy Technology Evaluation and Planning (KETEP) Grants funded by the Korea Ministry of Knowledge Economy (2013-101010-170C).

References

1. Finnis, M.W., *The theory of metal - ceramic interfaces.* Journal of Physics: Condensed Matter, 1996. **8**(32): p. 5811.
2. Sinnott, S.B. and E.C. Dickey, *Ceramic/metal interface structures and their relationship to atomic- and meso-scale properties.* Materials Science and Engineering: R: Reports, 2003. **43**(1–2): p. 1-59.
3. Clarke, D. and C. Levi, *Materials design for the next generation thermal barrier coatings.* Annual Review of Materials Research, 2003. **33**(1): p. 383-417.
4. Vaßen, R., et al., *Overview on advanced thermal barrier coatings.* Surface and Coatings Technology, 2010. **205**(4): p. 938-942.
5. Cao, X.Q., R. Vassen, and D. Stoever, *Ceramic materials for thermal barrier coatings.* Journal of the European Ceramic Society, 2004. **24**(1): p. 1-10.
6. Finnis, M., *The theory of metal-ceramic interfaces.* Journal of Physics: Condensed Matter, 1996. **8**(32): p. 5811.
7. Evans, A.G., et al., *Mechanisms controlling the durability of thermal barrier coatings.* Progress in Materials Science, 2001. **46**(5): p. 505-553.
8. Mumm, D. and A. Evans, *On the role of imperfections in the failure of a thermal barrier coating made by electron beam deposition.* Acta Materialia, 2000. **48**(8): p. 1815-1827.
9. Evans, A. and J. Hutchinson, *The mechanics of coating delamination in thermal gradients.* Surface and Coatings Technology, 2007. **201**(18): p. 7905-7916.
10. Guo, X. and F. Shang, *Shear strength and sliding behavior of Ni/Al 2 O 3 interfaces: A first-principle study.* Journal of Materials Research, 2012. **27**(09): p. 1237-1244.
11. Christensen, A. and E.A. Carter, *Adhesion of ultrathin ZrO2 (111) films on Ni (111) from first principles.* Journal of Chemical Physics, 2001. **114**(13): p. 5816-5831.
12. Arakere, N.K. and G. Swanson. *Effect of crystal orientation on fatigue failure of single crystal nickel base turbine blade superalloys*. in *ASME Turbo Expo 2000: Power for Land, Sea, and Air*. 2000. American Society of Mechanical Engineers.
13. Kresse, G. and J. Furthmüller, *Efficient iterative schemes for ab initio total-energy calculations using a plane-wave basis set.* Physical Review B, 1996. **54**(16): p. 11169-11186.
14. Kresse, G. and J. Furthmüller, *Efficiency of ab-initio total energy calculations for metals and semiconductors using a plane-wave basis set.* Computational Materials Science, 1996. **6**(1): p. 15-50.
15. Kresse, G. and J. Hafner, *Ab initio molecular dynamics for liquid metals.* Physical Review B, 1993. **47**(1): p. 558.
16. Hohenberg, P. and W. Kohn, *Inhomogeneous electron gas.* Physical review, 1964. **136**(3B): p. B864.
17. Kohn, W. and L.J. Sham, *Self-Consistent Equations Including Exchange and Correlation Effects.* Physical Review, 1965. **140**(4A): p. A1133-A1138.
18. Zhang, M., et al., *Hardness of FeB4: Density functional theory investigation.* The Journal of Chemical Physics, 2014. **140**(17): p. 174505.
19. Bader, R.F., *Atoms in molecules.* Accounts of Chemical Research, 1985. **18**(1): p. 9-15.
20. Henkelman, G., A. Arnaldsson, and H. Jónsson, *A fast and robust algorithm for Bader decomposition of charge density.* Computational Materials Science, 2006. **36**(3): p. 354-360.
21. Tang, W., E. Sanville, and G. Henkelman, *A grid-based Bader analysis algorithm without lattice bias.* Journal of Physics: Condensed Matter, 2009. **21**(8): p. 084204.
22. Ogata, S., et al. *Ab Initio Study of Ideal Shear Strength*. in *IUTAM Symposium on Mesoscopic Dynamics of Fracture Process and Materials Strength*. 2004. Springer.

23. Ledbetter, H. and R.P. Reed, *Elastic Properties of Metals and Alloys, I. Iron, Nickel, and Iron-Nickel Alloys.* Journal of Physical and Chemical Reference Data, 1973. **2**(3): p. 531-618.
24. Becke, A.D. and K.E. Edgecombe, *A simple measure of electron localization in atomic and molecular systems.* The Journal of Chemical Physics, 1990. **92**(9): p. 5397-5403.
25. Silvi, B. and A. Savin, *Classification of chemical bonds based on topological analysis of electron localization functions.* Nature, 1994. **371**(6499): p. 683-686.
26. Guo, X., et al., *Thermal Properties, Thermal Shock, and Thermal Cycling Behavior of Lanthanum Zirconate-Based Thermal Barrier Coatings.* Metallurgical and Materials Transactions E, 2016. **3**(2): p. 64-70.
27. Guo, X., et al., *Image-based multi-scale simulation and experimental validation of thermal conductivity of lanthanum zirconate.* International Journal of Heat and Mass Transfer, 2016. **100**: p. 34-38.